ADVANCED MATERIALS

www.advmat.de

A Room-Temperature Ferroelectric Ferromagnet in a 1D Tetrahedral Chain Network

*Kyeong Tae Kang, Chang Jae Roh, Jinyoung Lim, Taewon Min, Jun Han Lee, Kyoungjun Lee, Tae Yoon Lee, Seunghun Kang, Daehee Seol, Jiwoong Kim, Hiromichi Ohta, Amit Khare, Sungkyun Park, Yunseok Kim, Seung Chul Chae, Yoon Seok Oh, Jaekwang Lee, Jaejun Yu, Jong Seok Lee, and Woo Seok Choi**

Ferroelectricity occurs in crystals with broken spatial inversion symmetry. In conventional perovskite oxides, concerted ionic displacements within a 3D network of transition-metal–oxygen polyhedra (MO_x) manifest spontaneous polarization. Meanwhile, some 2D networks of MO_x foster geometric ferroelectricity with magnetism, owing to the distortion of the polyhedra. Because of the fundamentally different mechanism of ferroelectricity in a 2D network, one can further challenge an uncharted mechanism of ferroelectricity in a 1D channel of MO_x and estimate its feasibility. Here, ferroelectricity and coupled ferromagnetism in a 1D FeO_4 tetrahedral chain network of a brownmillerite $SrFeO_{2.5}$ epitaxial thin film are presented. The result provides a new paradigm for designing low-dimensional MO_x networks, which is expected to benefit the realization of macroscopic ferro-ordering materials including ferroelectric ferromagnets.

Complex transition-metal oxides can be analytically viewed as a network of transition-metal–oxygen polyhedra (MO_x) (**Table 1**). A collective distortion of such networks in a (quasi) 2D space can lead to inversion symmetry breaking and geometric ferroelectricity through trilinear coupling among distortions and electric polarization.[1–6] In comparison with the conventional displacive-type ferroelectricity in a 3D space, e.g., relative shifts of the transition-metal cation or lone-pair ions, geometric ferroelectricity does not require strong hybridization between the transition-metal and oxygen ions.[7–10] This removes the constraint of d^0-ness of the transition-metal ion, thereby allowing magnetism to coexist with ferroelectricity. In addition, while the soft-phonon mode at the Brillouin zone-center manifests displacive ferroelectricity,[11,12] the collective distortion of the 2D network results in zone-boundary soft-phonon modes for geometric ferroelectrics.[3]

What about in 1D networks? Spatial inversion symmetry breaking can be intuitively envisioned in 1D chain networks as well, especially with an MO_4 tetrahedral unit. An MO_4 tetrahedron has one of the lowest symmetries among the MO_x polyhedra and can form corner-shared 1D chains within crystals (Table 1). More interestingly, a collective distortion of the 1D network can introduce an unconventional polar state resulting from both the displacement of ions and the rotation of the tetrahedra.

Dr. K. T. Kang, Dr. A. Khare, Prof. W. S. Choi
Department of Physics
Sungkyunkwan University
Suwon 16419, Republic of Korea
E-mail: choiws@skku.edu

C. J. Roh, Prof. J. S. Lee
Department of Physics and Photon Science
Gwangju Institute of Science and Technology
Gwangju 61005, Republic of Korea

Dr. J. Lim, Prof. J. Yu
Department of Physics and Astronomy
Center for Theoretical Physics
Seoul National University
Seoul 08826, Republic of Korea

T. Min, J. Kim, Prof. S. Park, Prof. J. Lee
Department of Physics
Pusan National University
Busan 46241, Republic of Korea

J. H. Lee, Prof. Y. S. Oh
Department of Physics
Ulsan National Institute of Science and Technology
Ulsan 44919, Republic of Korea

K. Lee, T. Y. Lee, Prof. S. C. Chae
Department of Physics Education
Seoul National University
Seoul 08826, Republic of Korea

S. Kang, D. Seol, Prof. Y. Kim
School of Advanced Materials Science and Engineering
Sungkyunkwan University
Suwon 16419, Republic of Korea

Prof. H. Ohta
Research Institute for Electronic Science
Hokkaido University
Sapporo 001-0020, Japan

The ORCID identification number(s) for the author(s) of this article can be found under https://doi.org/10.1002/adma.201808104.

DOI: 10.1002/adma.201808104

Table 1. Classification of transition-metal oxide ferroelectrics based on the dimension of the polyhedra networks.

Network dimension	Unit polyhedron	Ferroelectric mechanism	Representative materials
3D network	Octahedron[a)]	Hybridization or lone pair	PZT, $BaTiO_3$, $BiFeO_3$, $BiMnO_3$
		Charge ordering	Fe_3O_4
		Magnetic ordering	Orthorhombic-$RMnO_3$ (R = Gd, Tb, Dy)
2D network	Octahedron[b)]	Geometric distortion	Ruddlesden–Popper phases, $PbTiO_3/SrTiO_3$ superlattice, $Ca_3Ti_2O_7$, K_2SeO_4, Cs_2CdI_4
	Triangular bipyramid[c)]	Geometric distortion	Hexagonal-$RMnO_3$ (R = Ho-Lu, Y), $LuFeO_3$
		Charge ordering	$LuFe_2O_4$
1D channel	Tetrahedron[d)]	Combined polar distortion	$SrFeO_{2.5}$

a)

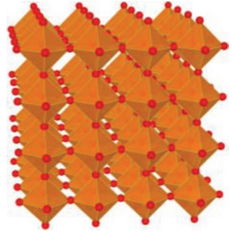

b)

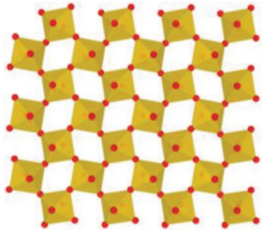

c)

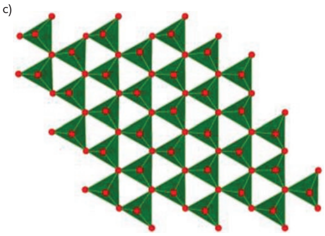

d)

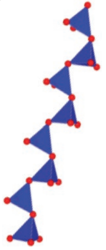

A combined polar distortion (CPD) can be considered as a trait of ferroelectricity in 1D channel systems, which can simultaneously introduce ferromagnetism. To realize the CPD within a 1D tetrahedral chain system, we fabricated an epitaxial brownmillerite $SrFeO_{2.5}$ thin film, which shows robust ferroelectricity with inversion symmetry breaking and CPD-induced coupled ferromagnetism.

Brownmillerite $SrFeO_{2.5}$ offers a 1D chain network of FeO_4 tetrahedra, in which two stable polarization states can be anticipated.[13–15] Orthorhombic $SrFeO_{2.5}$ possesses alternating layers of FeO_4 tetrahedra (blue) and FeO_6 octahedra (pink), which stack along the crystallographic b_o (subscript "o" denotes orthorhombic) axis, as schematically illustrated in **Figure 1**a. The FeO_4 tetrahedral chains are directed along the a_o axis. The epitaxial strain from the substrate and the thermodynamic parameters during the growth can be employed to determine the orientation of the brownmillerite crystal and FeO_4 tetrahedral chains.[16,17] Using pulsed laser epitaxy, we fabricated single-crystalline epitaxial $SrFeO_{2.5}$ thin films on cubic (Nb-doped) $SrTiO_3$ substrates with the following orientation relationships: $SrFeO_{2.5}$ $(\overline{1}01)_o//SrTiO_3$ $(001)_c$ and $SrFeO_{2.5}$ $[010]_o//SrTiO_3$ $[100]_c$ (subscript "c" denotes cubic) (Figure 1b,c). X-ray diffraction (XRD) θ–2θ scans, ω-scans, reciprocal space maps, and atomic force microscopy validated the expected structural orientation and high crystalline quality (refer Figure S1, Supporting Information). Within this configuration, the 1D tetrahedral chains are inclined by 45° to the surface normal of the substrate (Figure 1c).

The 1D tetrahedral chain network intrinsically conceives structural instability owing to the CPD provided by the brownmillerite structure. When imagining the rotation of an MO_x polyhedra, the axis of rotation should be defined. For the MO_6 octahedra or MO_5 triangular bipyramid, the apical oxygen and M ions are located in a line, which naturally serves as the rotation axis. This is not so trivial for the case of MO_4 tetrahedra owing to their low structural symmetry. In general, it will be natural to consider the transition-metal ion as the center of the rotation. However, within a crystal, e.g., brownmillerite, the alternate stacking of FeO_6 octahedral and FeO_4 tetrahedral layers anchors the positions of apical oxygen ions, and the line adjoining these ions serves as the rotation axis for each FeO_4 tetrahedron (insets of Figure 1d). With this rotation axis defined, CPD occurs naturally in 1D tetrahedral chains with rotational instability (refer Figure S2, Supporting Information). In addition to the collective polar rotation of the FeO_4 tetrahedra, the transition-metal ion has to simultaneously undergo a polar displacement with respect to the octahedral layer underneath. This essence of the CPD in the brownmillerite structure presents a stark contrast to the polar distortion in high-dimensional networks, where the polar cation displacement and polar rotation of the polyhedra are incompatible because of the preferential selection of distortive motion.[18]

When the CPDs of each chain exhibit the same handedness ($I2bm$ space group), polarization will emerge along the 1D tetrahedral chain direction, as shown in the insets of Figure 1d. The polarization value is theoretically estimated to be 7.77 $\mu C\ cm^{-2}$ by considering the relative displacement of ions (Figure S2, Supporting Information). Figure 1d describes the result of nudged elastic band (NEB) analysis for the examination of the lowest energy path between the two opposite polarization states, which theoretically supports the CPD-induced ferroelectricity in $SrFeO_{2.5}$. The highly symmetric $Imma$ space group is considered as a transition phase. The value of the switching barrier to reverse a tetrahedron is estimated to be ≈0.3 eV/tetrahedron. Although this value is larger than the values of the conventional ferroelectrics with tens of meV, it is comparable to geometric ferroelectrics with hundreds of meV.[19]

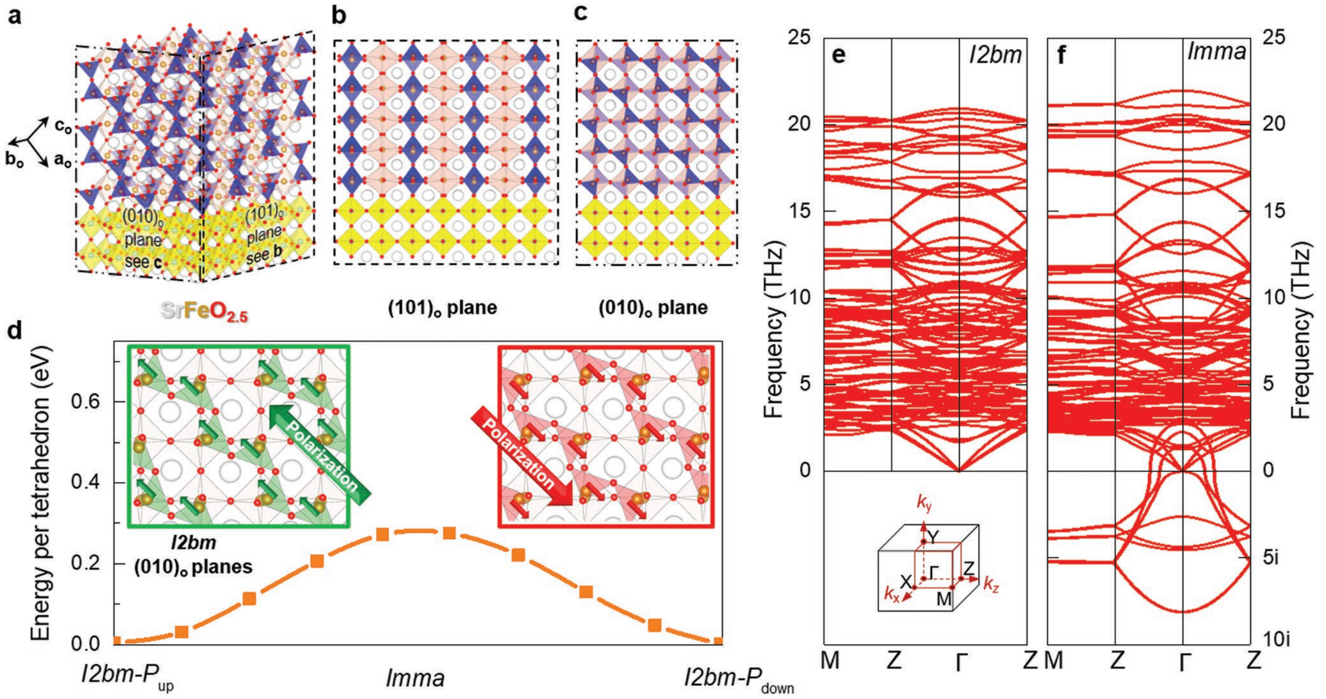

Figure 1. Brownmillerite $SrFeO_{2.5}$ with CPD in 1D tetrahedral chains. a) Schematic diagram of orthorhombic $SrFeO_{2.5}$ epitaxial thin film on a $SrTiO_3$ substrate with alternating FeO_4 tetrahedral (blue) and FeO_6 octahedral (pink) layers. b,c) Cross-sectional schematic views for the $(101)_o$ (b) and $(010)_o$ (c) planes. d) Minimized energetic path to reverse the 1D tetrahedral chain. The *I2bm* structure of $SrFeO_{2.5}$ in the left and right insets represents a polarized state, and the nonpolar symmetric *Imma* structure serves as a transition state. e,f) Phonon dispersion curves for ferroelectric *I2bm* (e) and unstable *Imma* (f) $SrFeO_{2.5}$ structures.

The CPD implies instabilities corresponding to both polar cation displacement and polar tetrahedral rotation. The two instabilities can be identified by the phonon dispersion relation. Figure 1e,f shows the theoretical phonon dispersion curves for the *I2bm* (low-temperature phase) and *Imma* (high-temperature phase) structures of $SrFeO_{2.5}$, respectively. Indeed, the *Imma* $SrFeO_{2.5}$ structure exhibits unstable (imaginary) soft modes all across the momentum space, including both the zone center and zone boundary. In particular, multiple dispersion curves can be identified, which might originate from the large structural degree of freedom based on the distortion of a 1D tetrahedral network. The soft-phonon modes at Z- (blue dot) and Γ-points (red dot) are shown in Figure S3b,c, in the Supporting Information, respectively. Both the modes exhibit the combined ionic motions of Fe displacement and tetrahedral rotation expected from previous IR spectroscopic measurements.[20] Considering the negligible octahedral distortion in the system, the CPD within the tetrahedral chains indeed plays an essential role for the emergent ferroelectricity.[21] We note that the silicate chain in Bi_2SiO_5 has been shown to exhibit polar rotation,[22,23] but without the fixed apical oxygen ions as in the brownmillerite structure of $SrFeO_{2.5}$.

The second-harmonic generation (SHG) measurements demonstrate the CPD-induced inversion symmetry breaking in the epitaxial $SrFeO_{2.5}$ thin film (**Figure 2**a–c).[24] Because our thin film is designed to have 1D tetrahedral chains oriented in a direction diagonal to the surface normal (Figure 1), polarization along both the in-plane and out-of-plane directions is anticipated. Clear SHG signals for the S_{in}–S_{out} (Figure 2a) and P_{in}–P_{out} (Figure 2b) configurations manifest the simultaneous inversion symmetry breaking along the in-plane and out-of-plane directions, respectively. The normal-incident SHG measurement further describes the domain structure with a particular point group symmetry. When defining the normal-incident beam polarization parallel to the a_c and b_c axes as X and Y, respectively, the φ-dependent SHG intensity of X_{in}–X_{out} and X_{in}–Y_{out} exhibits a fourfold symmetry, as shown in Figure 2c. The particular shape of the φ-dependent SHG result can be well fitted based on the point group symmetry *mm*2 of the expected *I2bm* structure, for both the X_{in}–X_{out} and X_{in}–Y_{out} configurations. The fitting suggests an area ratio of 4.6:5.4 between the domains of b_o // a_c and b_o // b_c, which stems from the structural degeneracy offered by the cubic substrate. Indeed, the macroscopic (micrometer)-scale structural domains with a phase difference of 90° are clearly visible on the surface of the $SrFeO_{2.5}$ thin film in the polarized optical microscopy images (refer to Figure S4g, Supporting Information). Although the domain structure might reduce the net magnitude of the in-plane polarization, the out-of-plane polarization is expected to remain robust.

The CPD-induced spatial inversion symmetry breaking leads to switchable ferroelectricity. Figure 2d shows the hysteretic polarization versus electric field curve of the $SrFeO_{2.5}$ epitaxial thin film, indicating robust ferroelectricity at room temperature (black line). The loop is obtained by the junction switching current (red line), which shows a peak near the coercive field (details in the Experimental Section). Despite the leaky nature of the switching current, a remnant polarization of 3 μC cm^{-2}

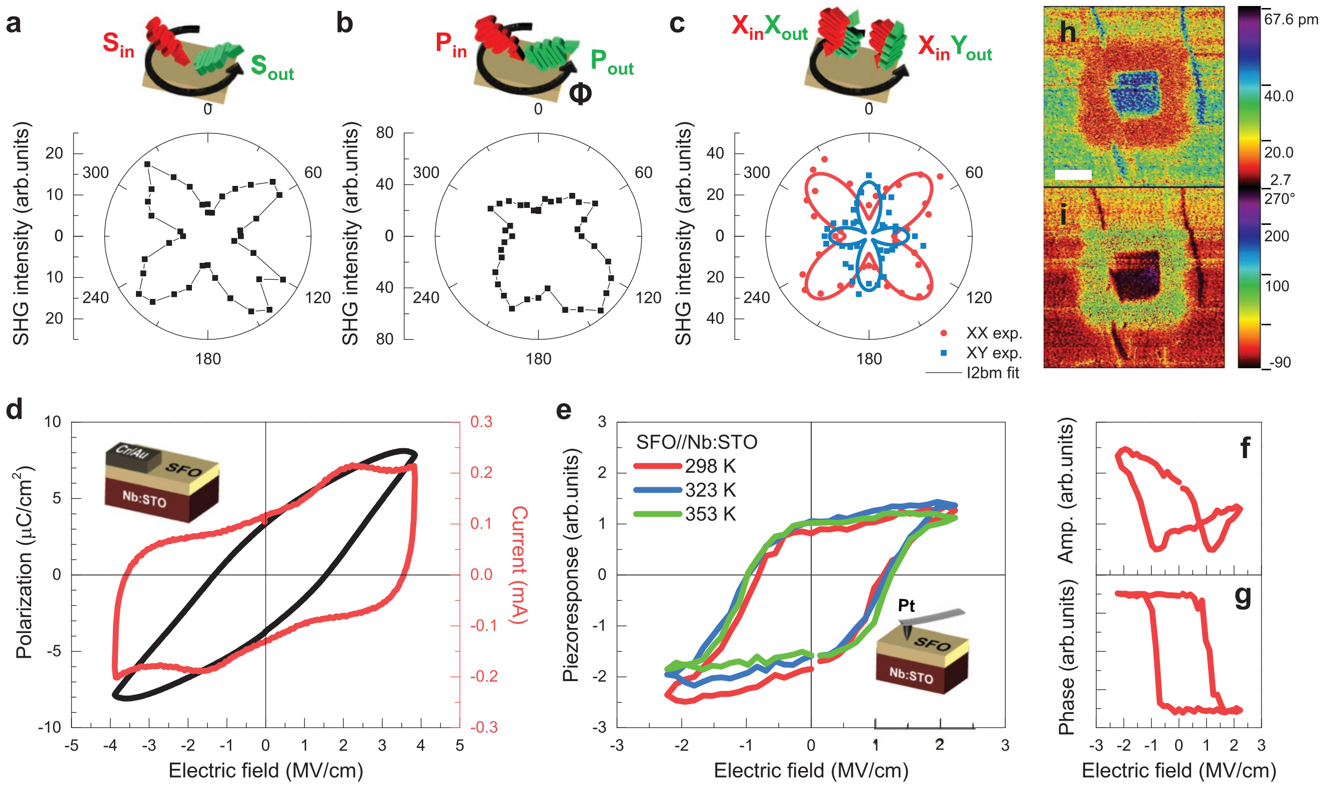

Figure 2. Ferroelectricity in the brownmillerite epitaxial thin film. a) S_{in}–S_{out} (in-plane) and b) P_{in}–P_{out} (out-of-plane symmetry breaking) configuration of the SHG signal. c) Normal-incidence SHG signal (dots) and its fit (solid lines) based on the *I2bm* $SrFeO_{2.5}$, where the a_c-parallel and b_c-parallel polarization geometries are denoted as X and Y, respectively. d) Polarization (black) and junction current (red) as a function of electric field for the epitaxial $SrFeO_{2.5}$ thin film at room temperature. e) Hysteresis loop obtained by PFM measurement at 298, 323, and 353 K. The insets show the schematic experimental configurations. f,g) Piezoresponse amplitude (f) and phase (g) as a function of electric field. h,i) Box-patterned PFM images of amplitude (h) and phase (i).

with a large coercive field of 1.5 MV cm^{-1} is obtained, which is consistent with the theoretical estimation. In addition, piezoresponse force microscopy (PFM) was employed to minimize the effect of the leakage current. Figure 2e shows the apparent hysteresis loop of the piezoresponse with a coercive field of 1.25 MV cm^{-1}, which is consistent with the switching current measurement. The negative correlation between the loop size and temperature in the temperature-dependent PFM measurement eliminates the possible contribution from possible ionic conduction to the loop.[25,26] The piezoresponse amplitude and phase (Figure 2f,g, respectively) and the bipolar box pattern images for the amplitude and phase (Figure 2h,i, respectively) further yield clear ferroelectric characteristics.

The CPD in a 1D tetrahedral network promotes ferromagnetic ordering which is coupled to the polar order. In particular, the alternate displacive motion of Fe and O in the typically antiferromagnetic brownmillerite $SrFeO_{2.5}$ leads to the Dzyaloshinskii–Moriya (DM) exchange interaction, as illustrated in **Figure 3**a–c.[1,27] A finite Dzyaloshinskii vector ($\mathbf{D}_{ij}$), resultant from the CPD-induced ferroelectricity, stabilizes the ferromagnetic ground state (refer Supporting Information). Figure 3d demonstrates the hysteretic magnetization versus magnetic field at 300 K. A clear ferromagnetic hysteresis with a small coercive field of ±130 Oe (dashed vertical lines) and remnant magnetization of ≈0.01 μ_B/Fe is observed, indicating canted ferromagnetism. The magnetoelectric coupling between the polar and magnetic orders via CPD is quantitatively evaluated by AC magnetoelectric coupling measurements. Figure 3e shows the change in the AC magnetoelectric coupling constant $\Delta\alpha$ as a function of the DC magnetic field H at 300 K. The AC magnetoelectric coupling constant α is defined as $\alpha \equiv \delta P_{ac}/\delta H_{ac} = \delta Q_{ac}/(\delta H_{ac} \cdot A)$, where δP_{ac} and δQ_{ac} are the amplitude of modulated electric polarization and charge by the applied AC magnetic field δH_{ac}, respectively, and A is the area of the electrode. Eddy current (induced by the Faraday's law) contribution to α was ruled out by considering a 90° phase difference relative to the H_{ac} (Figure S5b, Supporting Information). $\Delta\alpha$ was obtained by subtracting constant α values from $\alpha(H)$ (Figure S5, Supporting Information). While α itself is already a straightforward indicator of the magnetoelectric coupling, the underestimated $\Delta\alpha$ exhibits a clear magnetoelectric hysteresis with the peak features corresponding to the ferromagnetic coercive fields, indicating the synchronized reversal of the polar and magnetic domains driven by the external magnetic field. Note that a relatively small $\Delta\alpha$ is ascribed to the compensated magnetoelectric effect, which results from multiple magnetoelectric domains and/or the thermal instability of structural distortion. This result manifests the realization of magnetoelectrically coupled ferroelectric ferromagnets at room temperature.[28] Thus, 1D tetrahedral networks provide an unprecedented platform for the engineering of low-dimensional nanoscale networks, thereby leading to coupled ferro-ordering.

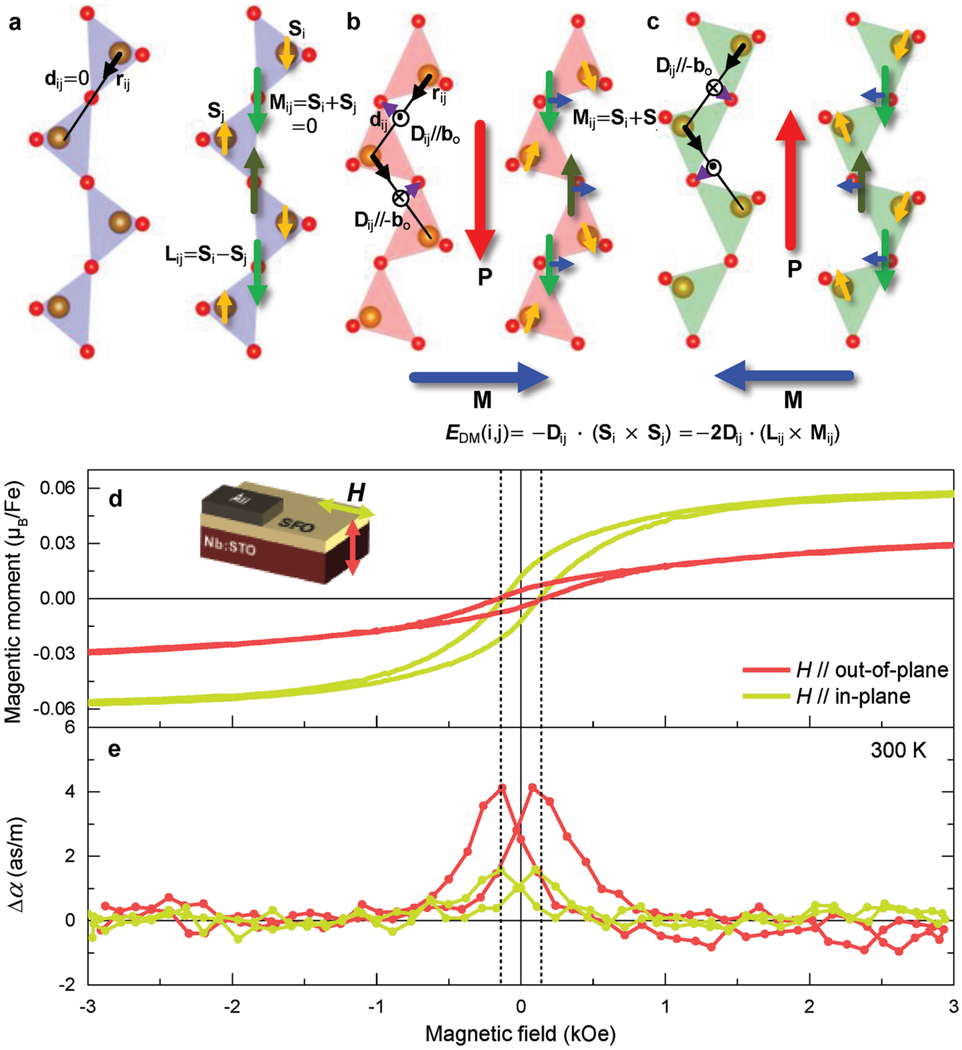

Figure 3. Room temperature ferromagnetism coupled with polarization. $\mathbf{r}_{ij}$ (black line) is the vector pointing towards a magnetic ion from a neighboring magnetic ion. $\mathbf{d}_{ij}$ (purple arrow) is the shift vector, which can be defined as the shift of oxygen ion from the line connecting magnetic ions. $\mathbf{L}_{ij}$ ($= \mathbf{S}_i - \mathbf{S}_j$, green arrows) is an antiferromagnetic vector defined as the difference between the spin vectors ($\mathbf{S}_i$ and $\mathbf{S}_j$, yellow arrows) of neighboring sites. $\mathbf{D}_{ij}$ is the Dzyaloshinskii vector pointing either towards the page or outwards from the page. $\mathbf{M}_{ij}$ ($= \mathbf{S}_i + \mathbf{S}_j$, blue arrows) is the local magnetic moment. a) When CPD is not present, $\mathbf{d}_{ij} = 0$; hence, $\mathbf{D}_{ij}$ and $\mathbf{M}_{ij}$ are all zero for the antiferromagnetically ordered spins parallel to the chain direction. b,c) When CPD occurs, the distortion within the tetrahedral chains gives rise to a finite $\mathbf{d}_{ij}$; hence, a collinear canting of the spins can be expected via the DM interaction. The resultant magnetization **M** is closely coupled to the electric polarization **P**. d,e) Ferromagnetism of epitaxial $SrFeO_{2.5}$ thin film magnetoelectrically coupled with electric polarization at room temperature. For both out-of-plane (red line) and in-plane (green line) magnetic fields, a magnetic hysteresis $M(H)$ and corresponding variation of magnetoelectric coupling constant $\Delta\alpha(H)$ are observed as a function of the applied DC magnetic field H. For $\Delta\alpha(H)$, constant values of $\alpha_{//,0}$ and $\alpha_{\perp,0}$ were subtracted from $\alpha(H)$, as shown in Figure S5 in the Supporting Information. The vertical dashed lines represent the coercive field.

Experimental Section

Thin Film Growth and Structural Characterization: Epitaxial $SrFeO_{2.5}$ thin films were grown on atomically flat (001)-oriented single-crystalline $SrTiO_3$ substrates using pulsed laser epitaxy at 700 °C under 1 mTorr of oxygen partial pressure. For the electrical measurements, metallic Nb-doped (0.5 wt%) $SrTiO_3$ substrate was employed as the bottom electrode. An excimer (KrF) laser of 248 nm wavelength (IPEX 864, Lightmachinery, Nepean, Canada) with an energy fluence of 1.3 J cm^{-2} and a repetition rate of 4 Hz was used. The atomic structures and crystallinity of the epitaxial thin films were characterized using high-resolution XRD. The thickness of the thin films was determined as 36 nm, using X-ray reflectivity.

Density Functional Theory Calculation: Density functional theory calculations were performed using the Vienna Ab Initio Simulation Package (VASP).[29] The generalized-gradient-approximation Perdew–Burke–Ernzerhof (GGA-PBE) exchange-correlation functionals[30] and the projected augmented wave pseudopotentials were employed.[31] The onsite Coulomb repulsion for the Fe d electrons using the GGA+U method with the effective Hubbard interaction parameter of U = 3 eV in the Dudarev implementation was included.[32] The energy barrier to invert the polarization to the opposite direction was calculated using the NEB method[33] as implemented in VASP, and the macroscopic polarization was obtained by the Berry phase method.[34] Phonon calculations were employed using the PHONOPY code.[35,36] To activate non-analytical term correction for improving the precision, the Born effective charges and dielectric constants were obtained using the density functional perturbation theory.[37] The NEB and Berry phase calculations were performed with the energy cutoff for a plane wave basis set of 600 eV, and further, a brownmillerite supercell including 36 atoms corresponding to $\sqrt{2} \times \sqrt{2} \times 4$ perovskite cells with $6 \times 6 \times 2$ Monkhorst–Pack *k*-point grid was used. The lattice structures were relaxed until the forces converged within 0.01 eV Å^{-1}, while the energy criterion was 10^{-6} eV. Meanwhile, for the phonon calculations, both the *I2bm* and *Imma* phases were optimized with an energy cutoff of 500 eV and Γ-centered $4 \times 4 \times 2$ *k*-point grid meshes. The lattice structures were fully relaxed until the forces were less than 10^{-6} eV Å^{-1} and converged in energy to 10^{-9} eV per unit cell.

SHG Measurements: SHG is an efficient method to investigate the broken inversion symmetry nature of a material non-destructively. It is feasible because the nonzero components of the second-order susceptibility ($\chi^{(2)}$) tensor reflect the absence of spatial inversion symmetry in a medium.

The second-harmonic response at room temperature was monitored using a Ti-sapphire oscillator (Vitara-T) with a central wavelength of 800 nm. A femtosecond laser with a pulse width of 30 fs and a repetition rate of 80 MHz was used. The fundamental wave with a beam size of approximately 100 μm^2 was focused using a plano-convex lens with a focal length of 100 mm. Depending on the purpose, both the grazing incidence with an incident angle of 45° and the normal incidence were exploited. The full-angle variations of the polarization of the fundamental wave and second-harmonic wave were controlled using a half-wave plate and polarizer, respectively, by which the *P*- or *S*-wave was well defined. The second-harmonic intensity was detected using a photomultiplier tube.

Ferroelectric Polarization Measurement and PFM: Polarization measurements were performed using a TF analyzer 3000 (aixACCT systems Co., Germany) at room temperature. Electric pulses of 2 kHz were applied to switch and measure the polarization of the thin film. The junction conductance was measured for a Cr, Au//$SrFeO_{2.5}$/Nb (0.5 wt%):$SrTiO_3$ device. The Cr/Au pad and Nb:$SrTiO_3$ substrate served as the top and bottom electrodes, respectively, as depicted in the inset of Figure 2d. From the junction conductance, the polarization can be obtained by

$$I(t) = A \times \frac{dP(t)}{dt} + C \times \frac{dV(t)}{dt} + I_c \tag{1}$$

where $I(t)$ and $V(t)$ are the junction current and voltage, respectively, and I_C is the conductance current.[38] A high frequency of 2 kHz was exploited, which is required to measure a leaky thin film sample owing to the nonzero $3d^5$ electrons with a small band gap of ≈1.5 eV. To overcome the large conductance current during the direct polarization measurement, a tip-based approach was also used to firmly determine the ferroelectricity.

The piezoresponse measurements were performed using a commercial atomic force microscope (AFM) system (NX-10, Park Systems) equipped with a function generator and data acquisition systems (NI-PXIe 5122/5412, National Instruments) (inset of Figure 2e). The piezoresponse was measured by applying a DC voltage ranging from –8 to 8 V_{DC} with a band excitation waveform of 2 V_{AC} between 320 and 400 kHz to a conductive Pt/Cr-coated AFM tip (Multi75E-G, Budget Sensors) with a spring constant of 3 N m^{-1}. A commercial AFM heating stage (Temperature Control Stage 1, Park Systems) was used to increase the temperature of the samples during the measurements. A switchable polarization of the $SrFeO_{2.5}$ epitaxial thin film was observed with a clear hysteresis behavior of the d_{33} signal from the PFM measurements after applying –8 V to the tip at room temperature, as shown in Figure 2e. Figure 2f,g shows the piezoresponse amplitude–voltage butterfly curve and hysteretic phase loop of the thin films, respectively. Furthermore, the surface of the thin film was scanned with an electrically biased tip of ±6 V, in a 10×10 μm^2 area for a box-patterned poling. The negative (center of box) and positive (box-border) poling regions are clearly distinguished in the amplitude (Figure 2h) and phase (Figure 2i) maps.[39,40]

Characterization of Magnetic Properties in Thin Films: Magnetization measurements for the $SrFeO_{2.5}$ thin film were performed using a commercial SQUID magnetometer (MPMS-3, Quantum Design Inc.) by applying a maximum field of 0.5 T at 300 K. The magnetic moment was obtained by vibrating the samples at 12.8 Hz (VSM mode) using a scan length of 5 mm and an average time of 2 s. Measurement for the magnetic property of the thin film is schematically shown in the inset of Figure 3d.

Quantitative Determination of Magnetoelectric Coupling: In magnetoelectric materials, oscillation of externally applied magnetic field (δH_{ac}) produces modulation of electric polarization (δP_{ac}). The magnetoelectric coupling constant α is defined by $\alpha = \delta P_{ac}/\delta H_{ac}$. The unit of α is s m^{-1}, which comes from the unit of P_{ac} in C m^{-2} and of H_{ac} in A m^{-1} = C/(m·s). To determine α quantitatively, a homemade magnetoelectric susceptometer was developed. The physical property measurement system (Quantum Design) was employed to apply a DC magnetic field H. The AC magnetic field was applied by a pair of counterwound solenoid coils, which compensates for the stray magnetic field outside the solenoid coils and minimizes the magnetic field–induced electrical noise. A three-turned coil, which was calibrated to the AC magnetic field as a function of applied AC current and frequency, was employed to determine δH_{ac}. The gold electrode was used as the top electrode, while the Nb-doped $SrTiO_3$ substrate was used as the bottom electrode. The sample was positioned at the center of the solenoids. By oscillating δH_{ac} at a frequency of 1 kHz while applying H, electric polarization within the epitaxial film modulates with the same frequency of 1 kHz and an amount of $\delta P_{ac} = \delta Q_{ac}/A$, where δQ_{ac} and A are the amount of charge modulation and the area of the top electrode, respectively. δQ_{ac} was amplified and converted to the calibrated voltage signal δV_{ac} by a homemade charge amplifier and lock-in amplifier (Stanford Research SR830). Thus, α was estimated by $\alpha \equiv \delta P_{ac}/\delta H_{ac} = \delta Q_{ac}/(\delta H_{ac} \cdot A)$. For the transverse ⊥ and longitudinal // configurations, both AC and DC magnetic fields were applied along the in-plane and out-of-plane of the thin film, respectively. To rule out possible extrinsic contributions, such as thermally excited carriers and eddy current on the electrode for the measured values of α, $\Delta\alpha$, where constant values of $\alpha_{\perp,0}$ and $\alpha_{//,0}$ were subtracted, was presented. It manifests the explicit hysteretic behavior as illustrated in Figure 3e, despite the modest values of as/m = 10^{-18} s m^{-1}.

Supporting Information

Supporting Information is available from the Wiley Online Library or from the author.

Acknowledgements

The authors thank G. Catalan, H. Taniguchi, C. H. Kim, J. M. Rondinelli, and J. Young for their insightful discussion. This work was supported by the Basic Science Research Programs through the National Research Foundation of Korea (NRF) (NRF-2019R1A2B5B02004546, 2017R1A4A1015323, and 2018M3D1A1089406). A part of the work was supported by Dynamic Alliance for Open Innovation Bridging Human, Environment and Materials as well as the Network Joint Research Center for Materials and Devices. The SQUID measurement was performed at Core Research Facilities at Pusan National University.

Conflict of Interest

The authors declare no conflict of interest.

Keywords

1D tetrahedral networks, ferroelectricity, magnetoelectric coupling, multiferroicity, $SrFeO_{2.5}$

Received: December 16, 2018
Revised: April 10, 2019
Published online: April 29, 2019

[1] S.-W. Cheong, M. Mostovoy, *Nat. Mater.* **2007**, *6*, 13.
[2] E. Bousquet, M. Dawber, N. Stucki, C. Lichtensteiger, P. Hermet, S. Gariglio, J.-M. Triscone, P. Ghosez, *Nature* **2008**, *452*, 732.
[3] N. A. Benedek, J. M. Rondinelli, H. Djani, P. Ghosez, P. Lightfoot, *Dalton Trans.* **2015**, *44*, 10543.
[4] N. A. Benedek, C. J. Fennie, *Phys. Rev. Lett.* **2011**, *106*, 107204.
[5] Y. S. Oh, X. Luo, F.-T. Huang, Y. Wang, S.-W. Cheong, *Nat. Mater.* **2015**, *14*, 407.
[6] W. Eerenstein, N. D. Mathur, J. F. Scott, *Nature* **2006**, *442*, 759.
[7] J. M. Rondinelli, S. J. May, J. W. Freeland, *MRS Bull.* **2012**, *37*, 261.
[8] M. Dawber, K. M. Rabe, J. F. Scott, *Rev. Mod. Phys.* **2005**, *77*, 1083.
[9] M. Gu, K. Wang, Y. Wang, Q. Xie, H. Cai, G.-P. Zhang, X. Wu, *npj Quantum Mater.* **2016**, *1*, 16011.
[10] N. A. Hill, *J. Phys. Chem. B* **2000**, *104*, 6694.
[11] P. A. Fleury, J. F. Scott, J. M. Worlock, *Phys. Rev. Lett.* **1968**, *21*, 16.
[12] Y. Luspin, J. L. Servoin, F. Gervais, *J. Phys. C: Solid State Phys.* **1980**, *13*, 3761.
[13] M. Schmidt, S. J. Campbell, *J. Solid State Chem.* **2001**, *156*, 292.
[14] J. E. Auckett, A. J. Studer, N. Sharma, C. D. Ling, *Solid State Ionics* **2012**, *225*, 432.
[15] J. Lim, J. Yu, *Phys. Rev. B* **2018**, *98*, 085106.
[16] J. Young, J. M. Rondinelli, *Phys. Rev. B* **2015**, *92*, 174111.
[17] A. Khare, J. Lee, J. Park, G.-Y. Kim, S.-Y. Choi, T. Katase, S. Roh, T. S. Yoo, J. Hwang, H. Ohta, J. Son, W. S. Choi, *ACS Appl. Mater. Interfaces* **2018**, *10*, 4831.
[18] N. A. Benedek, C. J. Fennie, *J. Phys. Chem. C* **2013**, *117*, 13339.
[19] A. T. Mulder, N. A. Benedek, J. M. Rondinelli, C. J. Fennie, *Adv. Funct. Mater.* **2013**, *23*, 4810.
[20] S. Roh, S. Lee, M. Lee, Y.-S. Seo, A. Khare, T. Yoo, S. Woo, W. S. Choi, J. Hwang, A. Glamazda, K. Y. Choi, *Phys. Rev. B* **2018**, *97*, 075104.
[21] H. Tian, X.-Y. Kuang, A.-J. Mao, Y. Yang, H. Xiang, C. Xu, S. O. Sayedaghaee, J. Íñiguez, L. Bellaiche, *Phys. Rev. Mater.* **2018**, *2*, 084402.
[22] H. Taniguchi, A. Kuwabara, J. Kim, Y. Kim, H. Moriwake, S. Kim, T. Hoshiyama, T. Koyama, S. Mori, M. Takata, H. Hosono, Y. Inaguma, M. Itoh, *Angew. Chem., Int. Ed.* **2013**, *52*, 8088.
[23] D. Seol, H. Taniguchi, J.-Y. Hwang, M. Itoh, H. Shin, S. W. Kim, Y. Kim, *Nanoscale* **2015**, *7*, 11561.
[24] H. Yokota, R. Haumont, J.-M. Kiat, H. Matsuura, Y. Uesu, *Appl. Phys. Lett.* **2009**, *95*, 082904.
[25] D. Seol, J. Ahreum, H. M. Hyung, S. Seongrok, Y. T. Sup, C. W. Seok, J. H. Suk, S. Hyunjung, K. Yunseok, *Adv. Funct. Mater.* **2017**, *27*, 1701924.
[26] R. K. Vasudevan, N. Balke, P. Maksymovych, S. Jesse, S. V. Kalinin, *Appl. Phys. Rev.* **2017**, *4*, 021302.
[27] I. Kagomiya, Y. Hirota, K.-I. Kakimoto, K. Fujii, M. Shiraiwa, M. Yashima, A. Fuwa, S. Nakamura, *Phys. Chem. Chem. Phys.* **2017**, *19*, 31194.
[28] J. Wang, J. B. Neaton, H. Zheng, V. Nagarajan, S. B. Ogale, B. Liu, D. Viehland, V. Vaithyanathan, D. G. Schlom, U. V. Waghmare, N. A. Spaldin, K. M. Rabe, M. Wuttig, R. Ramesh, *Science* **2003**, *299*, 1719.
[29] G. Kresse, J. Furthmüller, *Phys. Rev. B* **1996**, *54*, 11169.
[30] J. P. Perdew, K. Burke, M. Ernzerhof, *Phys. Rev. Lett.* **1996**, *77*, 3865.
[31] G. Kresse, D. Joubert, *Phys. Rev. B* **1999**, *59*, 1758.
[32] S. L. Dudarev, G. A. Botton, S. Y. Savrasov, C. J. Humphreys, A. P. Sutton, *Phys. Rev. B* **1998**, *57*, 1505.
[33] G. Mills, H. Jónsson, G. K. Schenter, *Surf. Sci.* **1995**, *324*, 305.
[34] R. D. King-Smith, D. Vanderbilt, *Phys. Rev. B* **1993**, *47*, 1651.
[35] K. Parlinski, Z. Q. Li, Y. Kawazoe, *Phys. Rev. Lett.* **1997**, *78*, 4063.
[36] A. Togo, F. Oba, I. Tanaka, *Phys. Rev. B* **2008**, *78*, 134106.
[37] M. Gajdoš, K. Hummer, G. Kresse, J. Furthmüller, F. Bechstedt, *Phys. Rev. B* **2006**, *73*, 045112.
[38] D.-Y. Wang, C.-Y. Chang, *Jpn. J. Appl. Phys.* **2005**, *44*, 1857.
[39] A. Gruverman, D. Wu, H. Lu, Y. Wang, H. W. Jang, C. M. Folkman, M. Y. Zhuravlev, D. Felker, M. Rzchowski, C. B. Eom, E. Y. Tsymbal, *Nano Lett.* **2009**, *9*, 3539.
[40] H. Lu, C.-W. Bark, D. Esque de los Ojos, J. Alcala, C. B. Eom, G. Catalan, A. Gruverman, *Science* **2012**, *336*, 59.